ORIGINAL PAPER

Hydraulic Fracture Feature of Rock Under Unloading Based on Test and Numerical Simulation

Junyan Yang · Meixia Wang · Zongqing Zhou · Weimin Yang · Songsong Bai · Daosheng Zhang · Yang Geng · Pinglin Jiang · Xinwei Ji · Pengfei Lv

Abstract Water inrush results from excavation unloading and high water pressure coupling. To study the propagation mechanisms of hydraulic fracture and failure mode under unloading conditions, hydraulic fracturing tests and numerical simulations were carried out to study the effects of unloading rate, principal stress difference, and the angle of water-conducting cracks on crack propagation. The results showed that the failure mode is a splitting failure with a single crack under a low unloading rate, while the mode is a multi-crack failure under a high unloading rate. Rock fracture requires higher water pressure under slow unloading conditions, but the rupture time is shorter, and the energy release rate in the moment of failure is greater. During unloading with a low principal stress difference, when the angle between the prefabricated crack and the horizontal direction of the model $\theta < 45°$, the extension direction of hydraulic fracture is mainly controlled by the maximum principal stress direction. When $\theta > 45°$, the growth direction is controlled by the angle of the water diversion fissure. During unloading with a principal stress difference of 0, when $\theta \leq 30°$, the propagation of hydraulic fracture is more easily controlled by the water conduction fracture. During unloading with a high principal stress difference, when $\theta \geq 30°$, the maximum principal stress direction controls the propagation. The angle of the water-conducting fracture has little effect on the propagation direction of the main crack. The research in this paper is of great importance in studying the mechanism of water inrush disasters.

J. Yang · Z. Zhou · W. Yang · S. Bai · D. Zhang · Y. Geng
School of Qilu Transportation, Shandong University, Jinan 250061, Shandong, China

M. Wang (✉) · Z. Zhou (✉) · W. Yang
Geotechnical and Structural Engineering Research Center, Shandong University, Jinan 250061, Shandong, China
e-mail: 15066231361@163.com

Z. Zhou
e-mail: Zongqing.Zhou@sdu.edu.cn

P. Jiang · P. Lv
Beijing Urban Construction Design and Development Group Co., Limited, Beijing 100037, China

P. Jiang
School of Mechanics and Civil Engineering, China University of Mining and Technology, Beijing 100083, China

X. Ji
Beijing Urban Construction Rail Transit Construction Engineering Co., Ltd, Beijing 102600, China

1 Introduction

At present, China has become the country in which the largest number of tunnels has been built (Evbuomwan and Yu [2011]; Zhou et al. [2021]; Fan et al. [2023];

Gao et al. 2018). Groundwater inrush is often encountered in the construction of tunnels (Liang et al. 2016; Zhu and Li 2020; Abdollahi et al. 2021; Zhang et al. 2022). The essence of the water inrush disaster is the release of surrounding rock stress and the expansion of cracks in rock mass during tunnel excavation unloading. When the tunnel face is close to water-filled karst caves and other geological structures, the cracks will further expand and penetrate under high water pressure, ultimately leading to water inrush disasters (Wang et al. 2020; Li et al. 2021a; Talebmorad et al. 2022). Water inrush disaster is the result of the coupling effect of excavation unloading and high water pressure. Therefore, the research of hydraulic fracture characteristics of rock mass under unloading conditions is of great significance to studying the mechanism of water inrush disasters.

Some research on the unloading of rock mass shows that the unloading mode and path greatly influence the stress eigenvalue, deformation parameters, and fracture precursor information of rock mass in each deformation stage (Jiang et al. 2020; Cao et al. 2023; Sivakumar and Maji 2023). With the unloading of confining pressure, rock rheological characteristics are obvious (Li et al. 2010). Notably, linear strain softening and multi-stage micro-fractures will occur after the rock mass is broken under unloading (Huang et al. 2015). Furthermore, the intermediate principal stress unloading disturbance causes rock failure from tensile shear to splitting (Yin et al. 2019). In the aspect of fluid–structure coupling, the influence of fluid on rock rheology under unloading is studied (Zhao and Jiang 2021). The yield and brittle failure of rock mass are more likely to occur with the increase of pore pressure (Zhang et al. 2021; Liu et al. 2020). However, the rock fracture caused by the unloading of surrounding rock under high water pressure is not considered. In addition, the current research mainly focuses on the unloading creep of rock mass, while the unloading effect caused by tunnel excavation is rarely studied.

In recent years, much research on hydraulic fracturing mechanisms has been carried out through experiments and numerical simulations (Duan et al. 2023; Sivakumar and Maji 2023; Zhao et al. 2022). Ren et al. (2021) studied the hydraulic fracture propagation law. The results showed that maximum and minimum horizontal in situ stress and the difference in stress affect the direction of crack propagation. Liu

et al. (2017) studied the influence of the presence of natural fractures around the wellbore, the dimension and volumetric density of random natural fractures, and the horizontal differential stress on hydraulic fracture propagation geometry. Yang et al. (2020) carried out true triaxial hydraulic fracturing tests and numerical simulations to analyze the effects of perforation angles and natural fractures on fracture propagation. Cordero et al. (2020) investigated the impact of natural fractures, rock permeability, fluid viscosity, initial stress state, and intercepting angle on hydraulic fracturing. Ma et al. (2016) conducted hydraulic fracturing experiments to study the influence law of crustal stress on fracture pressure and hydraulic fracture. The results showed that the fracture opening decreased with the principal stress difference increasing. Zou et al. (2016) studied a numerical approach based on DEM to investigate HFN propagation in a layered and naturally fractured formation. However, the hydraulic fracture of rock mass under unloading conditions is not further analyzed. In terms of numerical simulations, existing research mainly analyzed the macroscopic fracture propagation morphology and fracture pressure of rock mass. The distribution characteristics of the stress field and contact force between particles after rock mass fracture are not considered.

In general, there is much research on the fracture characteristics of rock mass under unloading conditions. Still, most of them do not consider the influence of fluid on the rock fracture. Besides, the existing research fields mainly focus on unloading creep of rock mass and unloading to increase seepage of shale gas and coalbed gas, but few researches on the unloading effect caused by tunnel excavation. In this paper, taking the limestone as the research object, the hydraulic fracture tests of rock mass under different unloading rates and principal stress differences are carried out using a multi-functional rock mechanics testing machine and a hydraulic loading system. Based on the acoustic emission device, the propagation form of the fracture surface, acoustic emission amplitude, and pump pressure curve of fractured rock mass are comprehensively analyzed. Further research is carried out based on PFC, including the fracture mode of rock mass and the propagation law of hydraulic fracture under different crack angles. The research in this paper is of great importance to study the mechanism of water inrush disasters.

2 Design of Test Scheme

2.1 Hydraulic Fracturing Experimental System

The whole test system is mainly composed of the following three parts.

2.1.1 Confining Pressure Loading System

It adopts the "tension–compression-shear" multifunctional rock mass testing machine independently developed by the Shandong University of China, which can realize the loading and unloading of different stress paths and synchronous output of stress–strain information (Li et al. 2021b).

2.1.2 Water Pressure Loading System

HPHS-100 high-pressure and high-speed servo pump is used in the water pressure loading system, which can provide a maximum water pressure of 100 MPa. It can realize two different water injection modes: constant pressure and constant flow. Besides, the real-time monitoring of water pressure changes in the hole can be realized through the computer control system.

2.1.3 Acoustic Emission Monitoring System

It adopts 8-channel AE monitoring equipment produced by the American Physical Acoustic Corporation (PAC), which is used to realize the three-dimensional location of hydraulic fractures and analyze the fracture signal. The device's sampling rate is as high as 10 MSPS, greatly improving the consistency between the collected and real waveforms.

2.2 Standard Sample Preparation

2.2.1 Sample Preparation

The rock used in the test was taken from a certain section of a diversion tunnel in Xinjiang, China. The original rock was cut, polished, and processed into a cube sample with a side length of 150 mm. A injection wellbore with a diameter of 10 mm and
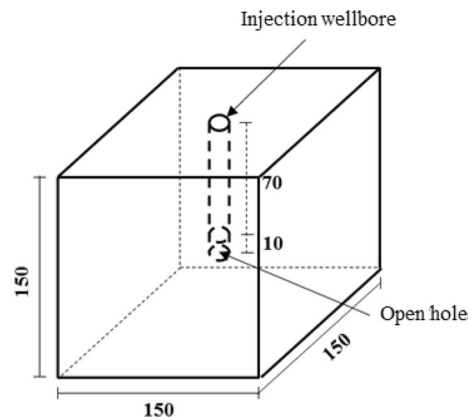

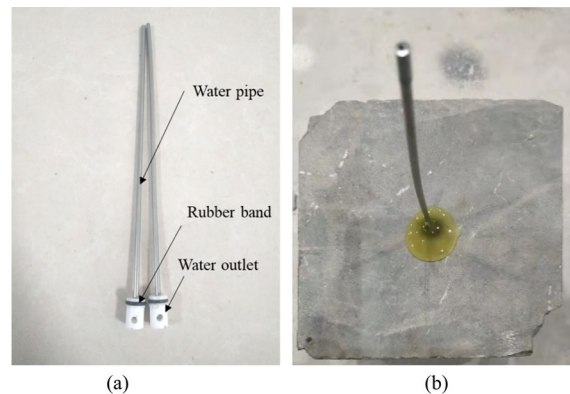**Fig. 1** Schematic diagram of standard sample for hydraulic fracture test (unit: mm)

Fig. 2 Sample sealing: **a** Prefabricated hole sealer; **b** Hole sealing

a depth of 80 mm was drilled vertically downward at the center of the top surface of the sample. And schematic diagram of standard sample for hydraulic fracture test is shown in Fig. 1.

2.2.2 Sample Sealing

The prefabricated hole sealing device and epoxy resin glue were used to seal the hole, aiming to realize the closed connection between the water injection hole and hydraulic loading system and prevent leakage and pressure relief phenomenon in the fracturing process. The prefabricated hole sealer had an outer diameter of 10 mm, an inner diameter of 7 mm, and a length of 70 mm (10 mm was reserved at the bottom of the hole as the open hole fracturing section). A slot is

prefabricated at the sealer bottom, and a rubber ring is installed to prevent epoxy resin from flowing into the open hole section, as shown in Fig. 2a. Before sealing, pour a small amount of magenta reagent into the bottom of the hole; then extend the sealer into the bottom; finally, evenly inject the epoxy resin glue into the wellbore and let it stand for 24 h. After the epoxy resin glue is fully solidified, the hole sealing is completed, as shown in Fig. 2b.

2.3 Overall Design of the Test

2.3.1 Design of Work Condition

The hydraulic coupling fracture test of rock mass under step-by-step unloading was carried out to explore the failure mode and crack propagation evolution law, taking the hydraulic fracturing test under constant confining pressure as a contrast. The unloading rate was 0.01 MPa/s to simulate the unloading process of TBM excavation (slow continuous unloading). The unloading rate was 0.1 MPa/s to simulate the unloading process of drilling and blasting excavation (rapid graded unloading). The test adopted the graded unloading to prevent the test phenomenon from being obvious due to the large unloading rate. The time that the stress remains constant was 10 s. The unloading stress path is shown in Fig. 3.

Since the propagation mode of hydraulic crack is mainly influenced by the horizontal in-situ stress distribution, vertical stress was not considered in this
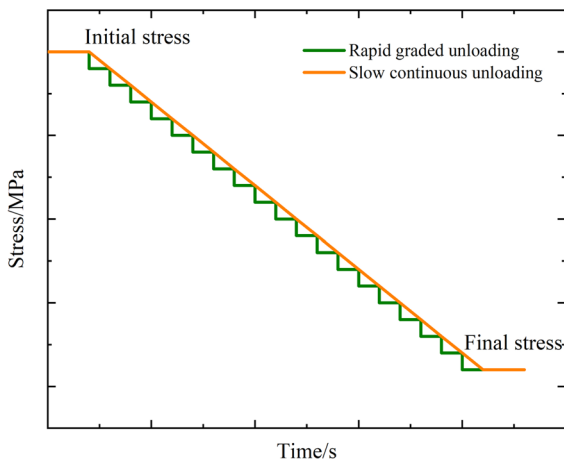
Table 1 Hydraulic coupling fracture condition design

Sample number	Initial stress (MPa)	Unloading rate (MPa/s)
1–1	$\sigma_H = \sigma_h = 5$	0
1–2		0.01
1–3		0.1
2–1	$\sigma_H = 5, \sigma_h = 8$	0
2–2		0.01
2–3		0.1

test design. Only the influence of horizontal two-way principal stresses σ_H and σ_h on the propagation mode was considered. The specific test plan is shown in Table 1.

2.3.2 Test Procedure

2.3.2.1 Installation of Sample Firstly, samples with sealed holes were placed on the test machine, and then the water injection hole was closely connected with the hydraulic loading system; secondly, two acoustic emission probes were installed on each side of the front, back, and left along the diagonal; lastly, the contact parts of the probe and the sample were smeared with vaseline.

2.3.2.2 In-Situ Stress Loading To ensure that the confining pressure is applied accurately and evenly on the sample surface, made the pressing plate contact with the sample by controlling the oil pressure loading system, then inputted the setting confining pressure in the control system, and finally made the confining pressure load to the specified value of the test.

2.3.2.3 Hydraulic Fracturing of Rock Mass Under Unloading Condition At first, the hydraulic fracture test under a fixed confining pressure should be carried out to determine the fracture pressure of the rock mass. At this time, the value slightly less than the fracture pressure was regarded as the constant hole water pressure, and the unloading test was carried out to study the fracture modes. Then, the hydraulic fracture test under the step-by-step unloading was carried out. The water injection pressure should be less than the fracture pressure under the constant confining pressure. The horizontal stress was unloaded at

Fig. 3 Schematic diagram of unloading stress path

the specified rate through the computer control system until the red fracturing fluid seeped out on the sample surface at a certain unloading pressure, indicating that the hydraulic fracture had penetrated through the whole rock sample. The fracturing was completed at this time. The entire hydraulic coupling fracture test device is shown in Fig. 4.

3 Analysis of Test Results

The fractured sample was observed and cut along the hydraulic fracture to obtain the expansion shape of the hydraulic fracture. Further, combined with
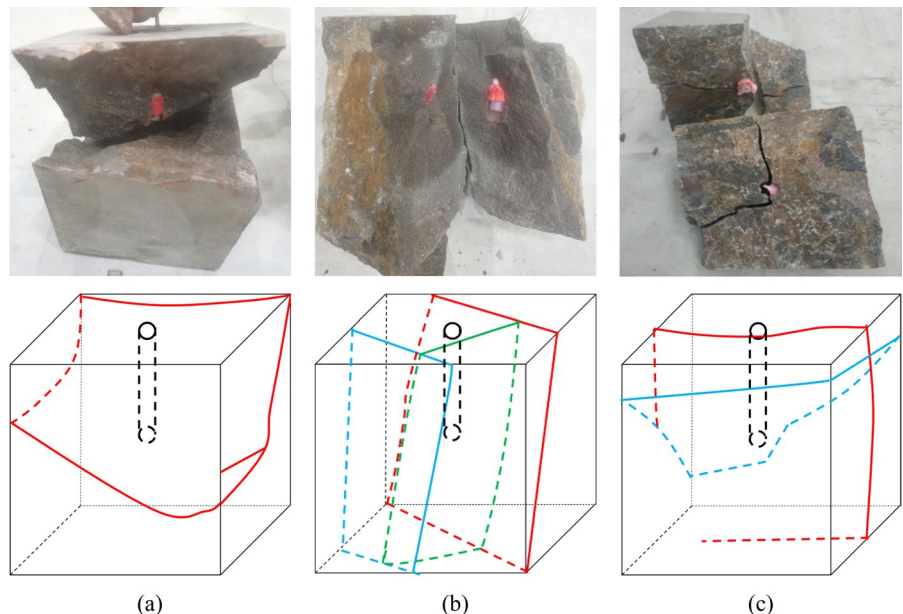
acoustic emission information, the crack propagation law under different working conditions was analyzed.

3.1 Initial Principal Stress $\sigma_H = \sigma_h = 5\text{MPa}$

When the initial principal stress difference is 0, the fracture morphology of rock mass under different unloading rates is shown in Fig. 5. When the unloading rate is 0, the hydraulic fracture is not induced by the direction of maximum principal stress, and it is easy to form a 45° inclined tension-shear fracture surface. When the unloading rate is 0.01 MPa/s, the principal stress difference is small at the initial stage of unloading, and multiple cracks appear at the bottom of the injection hole (Fig. 5a). With the decrease of σ_H, the principal stress difference increases gradually. Finally, three fracture surfaces are formed, which are in "H" shape distribution (Fig. 5b). Two parallel fracture surfaces deflect to the direction of the maximum principal stress and 30° to the direction of the maximum principal stress, mainly due to the induced by the maximum principal stress. The third fracture surface is perpendicular to the two fracture surfaces, mainly due to the stress shadow effect between the two hydraulic fractures. When the unloading rate is 0.1 MPa/s, induced by the maximum principal stress, a single tension fracture is formed along the direction of the maximum principal stress (Fig. 5c red line). Besides, a circumferential shear fracture is

Fig. 4 The whole hydraulic coupling fracture test device

Fig. 5 Fracture morphology and three-dimensional fracture distribution of rock mass under different unloading rates:: **a** No unloading; **b** Slow unloading; **c** Rapid unloading

(a)　　　　　(b)　　　　　(c)

formed (Fig. 5c blue line). It is speculated that the main reason is that the hydraulic fracture is captured by the natural fracture after the intersection and then propagates along the direction of the natural fracture. Therefore, compared with no unloading, the failure mode of rock mass under slow unloading is a multiple fracture cutting failure, and the hydraulic fracture deflects due to the slow increase of principal stress difference. However, the failure mode of rock mass under rapid unloading is tension shear failure of a single fracture.

Based on the AE amplitude in the fracturing process, the fracture process of rock mass has been analyzed in depth. Figure 6 shows the variation of AE amplitude and pump pressure curve of hydraulic fracture under slow unloading and rapid unloading. From the variation of AE amplitude, it can be seen that the micro-fractures start to crack, expand, and connect during the process of rock fracture. The AE amplitude reaches its peak value at the moment of fracturing, but there are differences in the amplitude variation under different unloading conditions. Under slow unloading, there is a single peak value with an amplitude of about 3500 dB, and the amplitude is low at other times (Fig. 6a). However, there are multiple amplitude peaks around 40 s and 200 s under rapid unloading, and the maximum peak value is about 1400 dB (Fig. 6b), which is much smaller than the AE amplitude at low unloading speed. It

shows that the energy stored in the rock mass is challenging to release quickly at a low unloading speed. When the unloading reaches a certain pressure, the water pressure in the hole will fracture the rock mass instantly, the internal stress of the rock mass is rapidly released, and there are few micro-cracks in the rock mass. However, the internal energy of the rock mass will be released rapidly in the process of rapid unloading, and a large number of micro-cracks will be generated in the rock mass. In Fig. 6b, a large AE amplitude appears in the later stage of rock mass fracture, mainly due to the initiation and propagation of branch fractures induced by unloading. This is consistent with the failure characteristics of surrounding rock under TBM and drilling blasting construction. Therefore, the rock failure test under unloading conditions can truly reflect the influence of different excavation methods on the stability of the surrounding rock.

The fracture pressure of rock mass under different working conditions has been analyzed based on the pump pressure curve. It can be seen from the pump pressure curve that the variation of the water pressure in the hole and the variation of the AE amplitude have a good consistency during the rock fracture process. The fracture pressure shows that the fracture pressure of rock mass under low unloading and high unloading speeds are 18 MPa and 10 MPa, respectively. Therefore, compared with high unloading, slow unloading requires higher water pressure for rock mass rupture, but the
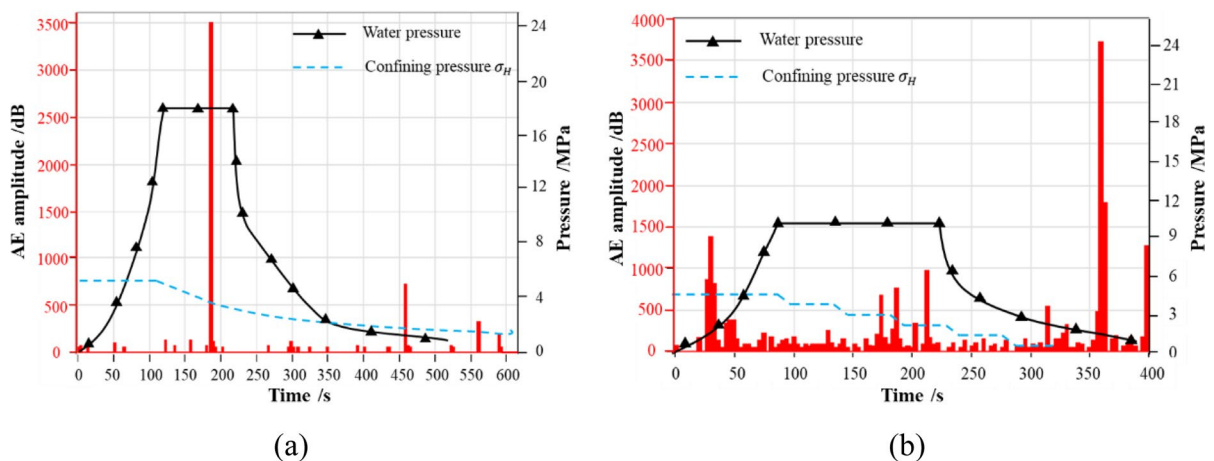

(a)

(b)

Fig. 6 Acoustic emission amplitude and pump pressure curve of hydraulic coupling fracture test: **a** Slow unloading; **b** Rapid unloading

rupture time is shorter, and the energy release rate in the moment of failure is greater.

## 3.2 Initial Principal Stress

$$\sigma_H = 5 \text{MPa and } \sigma_h = 8 \text{MPa}$$

When the unloading rate is 0, the principal stress difference is relatively small, and the fracture pattern is inclined on a three-dimensional surface, which is 45° with the maximum principal stress direction, as shown in Fig. 7a. Under the condition of slow unloading, the main fracture surface and maximum principal stress direction are basically 45°, as shown in Fig. 7b. It shows that the slow increase of the principal stress difference has little effect on the propagation direction of the main fracture surface at a low unloading speed. However, compared with no unloading, the fracture surface is larger and the fracture roughness is higher under the condition of slow unloading. Under the condition of rapid unloading, there are two mutually perpendicular fracture surfaces in the rock in Fig. 7c. The principal fracture surface I (red line) is straight and smooth, which directly passes through the injection hole to form a splitting fracture, showing two-dimensional plane expansion. The formation of branch fracture surface II (blue line) is mainly due to the hydraulic fracture connecting with the natural joint surface and extending along with it. Therefore,

under the condition of initial principal stress $\sigma_H < \sigma_h$, the propagation surface of hydraulic fracture is relatively single and basically expands along the direction of the maximum principal stress. However, compared with the condition without unloading, the main fracture surface becomes a three-dimensional curved surface at a low unloading speed, and the fracture area of the rock mass is larger. The principal fracture surface is flat and smooth at a high unloading speed and expands in a two-dimensional plane.

The changes in acoustic emission amplitude and pump pressure curve of rock mass hydraulic coupling fracture under different unloading speeds are shown in Fig. 8. It can be seen from Fig. 8a that there are several peak amplitude values after 150 s under slow unloading, and the peak strength is about 5000 dB. It is mainly due to the weak induction effect of principal stress difference on hydraulic fracture under slow unloading. Micro-fractures are easy to occur in the fracturing process, and the hydraulic fracture surface is rough and tortuous. On the contrary, the AE amplitude has two high peaks when unloading rapidly, which are around 120 s and 300 s respectively (Fig. 8b). The peak value of AE amplitude at 120 s is mainly due to the initiation and propagation of micro-cracks in rock mass under the initial high principal stress difference. The peak value of AE amplitude reaches 8800 dB near 300 s, mainly due to the principal stress σ_H decreasing

Fig. 7 Fracture morphology and three-dimensional fracture distribution of rock mass under different unloading rates:: **a** No unloading; **b** Slow unloading; **c** Rapid unloading
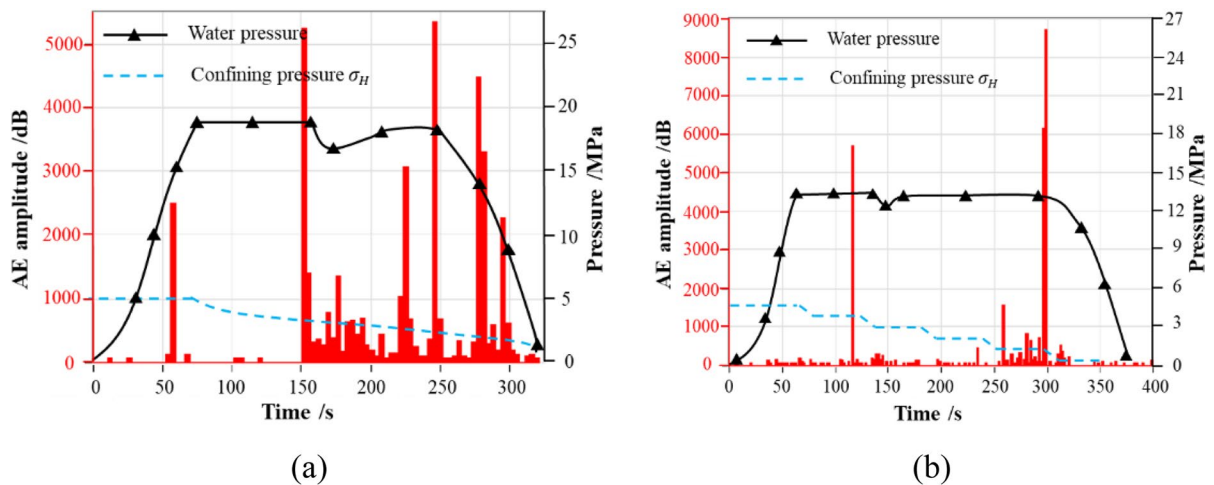
(a)   (b)   (c)
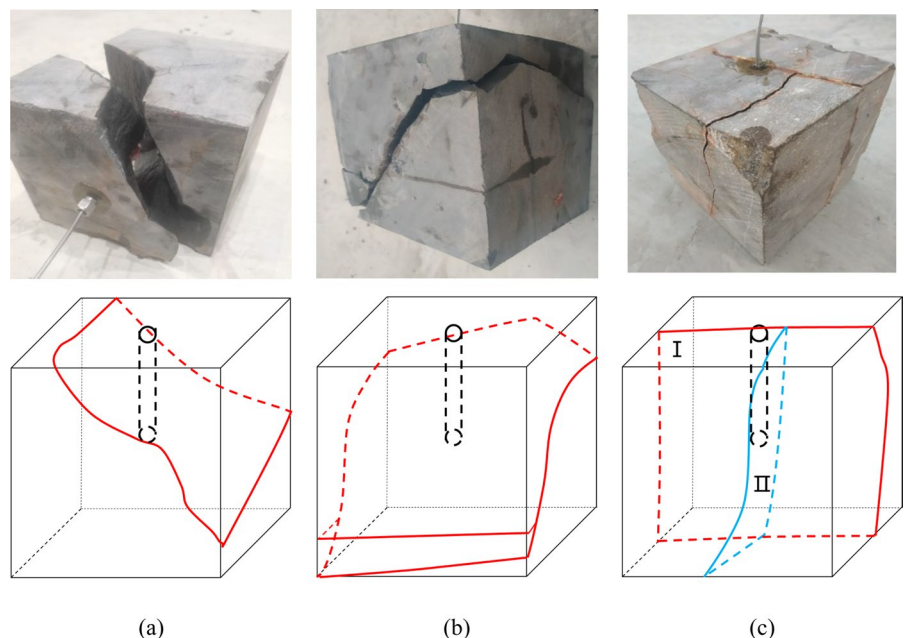
Fig. 8 Acoustic emission amplitude and pump pressure curve of hydraulic coupling fracture test: **a** Slow unloading; **b** Rapid unloading

rapidly and tending to 0 under high unloading speed. At this time, the induction effect of the maximum principal stress is significantly enhanced, and the new cracks in the rock mass rapidly initiate and expand and join with the old hydraulic fractures, forming a complex fracture network in the rock mass. The failure mode of the rock mass is transformed into multi-fracture cutting failure.

According to the pump pressure curve, the fracture pressure of rock mass under low and high loading speeds is 18 MPa and 13 MPa, respectively, in Fig. 8. It shows that the fracture pressure of rock mass decreases gradually with the increase in the unloading rate. The main reason is that the principal stress difference increases gradually with the acceleration of σ_H the reduction rate, and the induction effect of the maximum principal stress becomes more and more intense, thus accelerating the fracture of the rock mass.

4 Hydraulic Coupling Simulation of Rock Fracture Under Unloading Condition

4.1 Calibration of Macro and Micro Parameters

The correct selection of micro parameters is the key to numerical analysis. To ensure the accuracy of the numerical model, firstly, the conventional mechanical parameters of the limestone were obtained through a series of tests, including the Brazilian splitting test, uniaxial compression test, and triaxial compression test. The parameters values are shown in Table 2.

Then, cylinder models corresponding to the tests were established in the PFC^{2D} program. The cylinder dimensions are 50 mm × 100 mm and 50 mm × 25 mm (diameter × height). The minimum radius of particles R_{min} is 0.8 mm, and the maximum radius R_{max} is 1.2 m, with a uniform distribution. The density of the model is 2445 kg/m^3, and the porosity is set to 0.15. The contact model between particles adopts the flat-jointed model (FJM) that can describe the finite size, linear elasticity, and local damage of rock mass. In FJM, there are five main parameters to be calibrated. The parameters are

Table 2 Basic mechanical parameters of raw rock

Mechanical parameter	Density (kg/m^3)	Compressive strength (MPa)	Elasticity modulus (GPa)	Poisson's ratio	Tensile strength (MPa)	Cohesion (MPa)	Friction angle (°)
Value	2445	120	20	0.19	7.36	14.7	62

tangential bond strength, normal bond strength, stiffness ratio, deformation modulus, and Internal friction angle. Brazilian splitting simulation is used to calibrate the normal bond strength. Uniaxial compression simulation is used to calibrate the tangential bond strength, stiffness ratio, and deformation modulus. Based on the conventional mechanical parameters of the limestone in Table 2, the numerical simulation of the basic mechanical test is carried out. The values of five micro parameters are obtained by trial and error method. Through constant parameter debugging, the final model failure mode and stress−strain curve are shown in Fig. 9 and Fig. 10. It can be seen that the numerical simulation results are in good agreement with the test results. Finally, the micro parameters are shown in Table 3.

4.2 Correctness Verification of Numerical Models

It is necessary to calibrate the fluid flow characteristic parameters and verify the correctness of the numerical model in addition to the rock mechanics parameters. The dimensions of the model are 150 mm × 150 mm. The minimum radius of particles R_{min} is 0.8 mm, and the maximum radius R_{max} is 1.2 m, with a uniform distribution. The diameter of the water injection hole is 10 mm, and 18,164 particles are generated in the end. The fluid–solid two-way coupling is realized by using the pipeline-domain model. The numerical calculation model is shown in Fig. 11.

Fig. 9 Comparison of Brazilian splitting simulation results and laboratory test results: Comparison of Brazilian splitting simulation results and laboratory test results **a** Failure mode; **b** Stress−strain curve
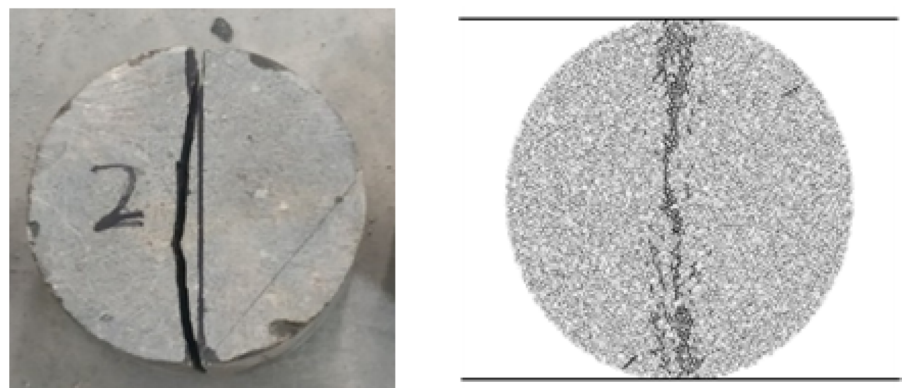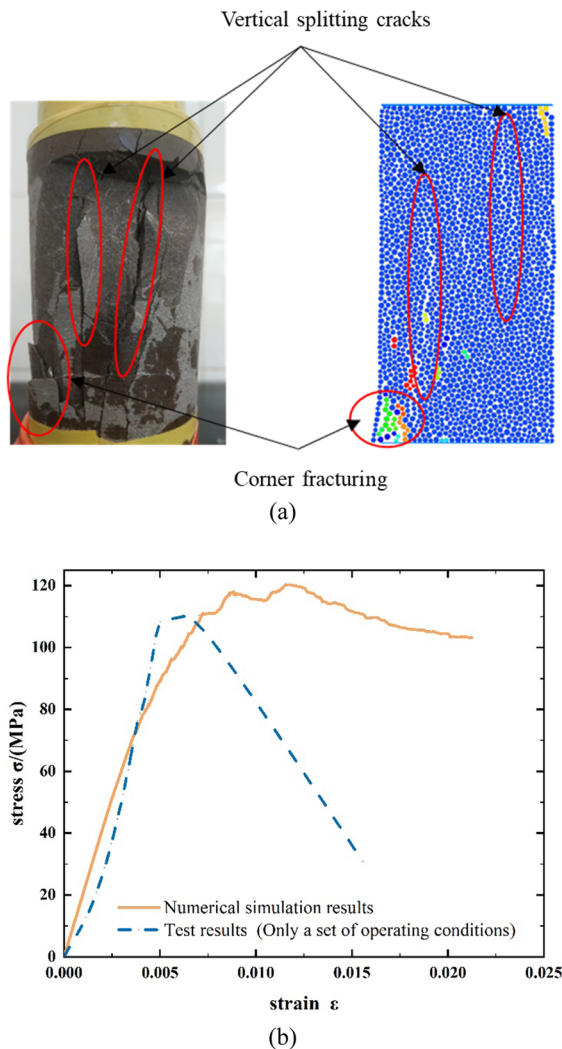

(a)
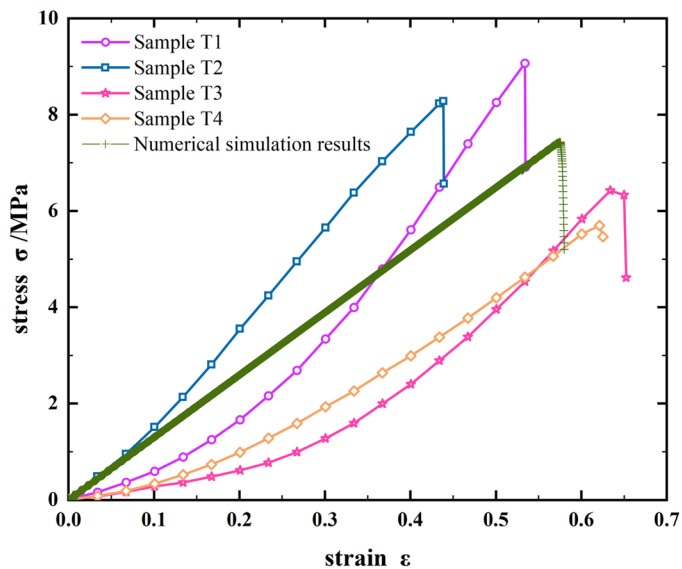
(b)

Fig. 10 Comparison of Uniaxial compression simulation results and laboratory test results: **a** Failure mode; **b** Stress−strain curve

After the numerical model was established, the fluid parameters needed to be calibrated to realize the two-way coupling between particles and fluid. In the design of simulated working conditions, the initial principal stress was considered as $\sigma_H = \sigma_h = 5$ MPa, $\sigma_H = 5$ MPa and $\sigma_h = 8$ MPa. The unloading rates were 0 and 0.01 MPa/s, respectively. After dozens of groups of simulation debugging, the fracture morphology of the four models under a set of parameters was obtained. The comparison of fracture morphology between the simulation and the test is shown in Fig. 12. The propagation model of hydraulic fracture shows that when the initial principal stress $\sigma_H = \sigma_h = 5$ MPa, the main controlling vertical fracture was formed at the slow unloading (0.01 MPa/s). It is consistent with the surface of the main vertical fracture obtained from the test. When the initial principal stress $\sigma_H = 5$ MPa and $\sigma_h = 8$ MPa, a broken line through the main fracture was formed without unloading. At the same time, a hydraulic fracture along the vertical direction was formed at the slow unloading, and a branch fracture was formed at the orifice, which was in good agreement with the hydraulic fracture propagation obtained from the test. Therefore, the numerical model established by this set of parameters can simulate the rock's hydraulic coupling fracture process. Finally, the fluid parameters of the model are shown in Table 4.

4.3 The Scheme of Numerical Simulation

Under the unloading conditions, to consider the fracture mechanism of rock mass with prefabricated water conducting crack, this study aimed to reveal the influence of water-conducting fissures on the propagation form of hydraulic fracture, and then provided some theoretical guidance for the prevention and control of water inrush during tunnel construction. Therefore,

Table 3 The micro parameters

| Particle properties	Parameter values	Contact properties	Parameter values
Elastic modulus E_c/(Pa)	10e9	Deformation modulus E_d/(GPa)	12
Stiffness ratio k_n/k_s	2.0	Stiffness ratio k_n/k_s	2.13
Porosity n	0.15	Normal bond strength n_bond/(MPa)	1.6e7
Density ρ/(kg · m^{-3})	2445	Tangential bond strength s_bond/(MPa)	4.9e7
Damping C/(N/(m · s^{-1}))	0.7	Internal friction angle φ(°)	62°
Friction coefficient	0.5	Friction coefficient	1.6
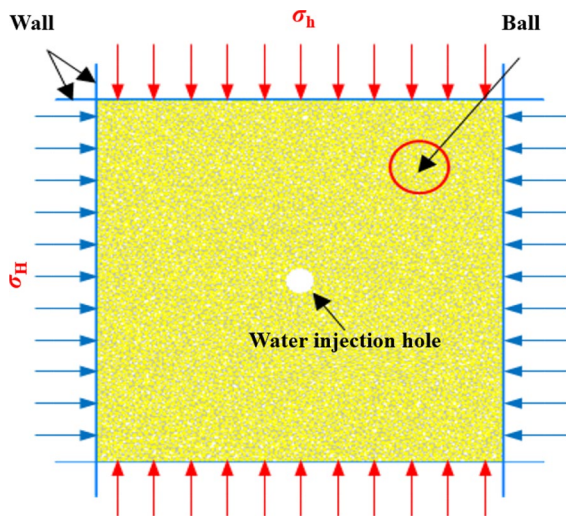
Fig. 11 Numerical calculation model of hydraulic coupling fracture

the angle of the water-conducting crack and the principal stress difference were used as the research object to explore the fracture mode of rock mass under their influence. A crack with a length of 20 mm and a width of 1.5 mm was prefabricated at the water

injection hole. The angle between the prefabricated crack and the horizontal direction of the model is denoted as θ. The values of θ are 0°, 15°, 30°, 45°, 60°, and 90°. A total of 18 working conditions were set, and the specific conditions are shown in Table 5. The numerical simulation model of hydraulic coupling fracture of rock mass with prefabricated crack is shown in Fig. 13.

5 Analysis of Numerical Simulation Results

5.1 Analysis of Hydraulic Fracture Propagation

The fracture propagation mode of hydraulic coupling simulation under the different initial principal stress and the angle of the water-conducting crack are shown in Fig. 14. As shown in Fig. 14(a), when the initial principal stress $\sigma_H = 5$ MPa and $\sigma_h = 2$ MPa, the maximum principal stress direction is along the horizontal direction. When $\theta < 45°$, the hydraulic fracture is induced by the maximum principal stress after cracking from the tip of the water-conducting fracture. During the expansion process, it does not expand along the direction of the
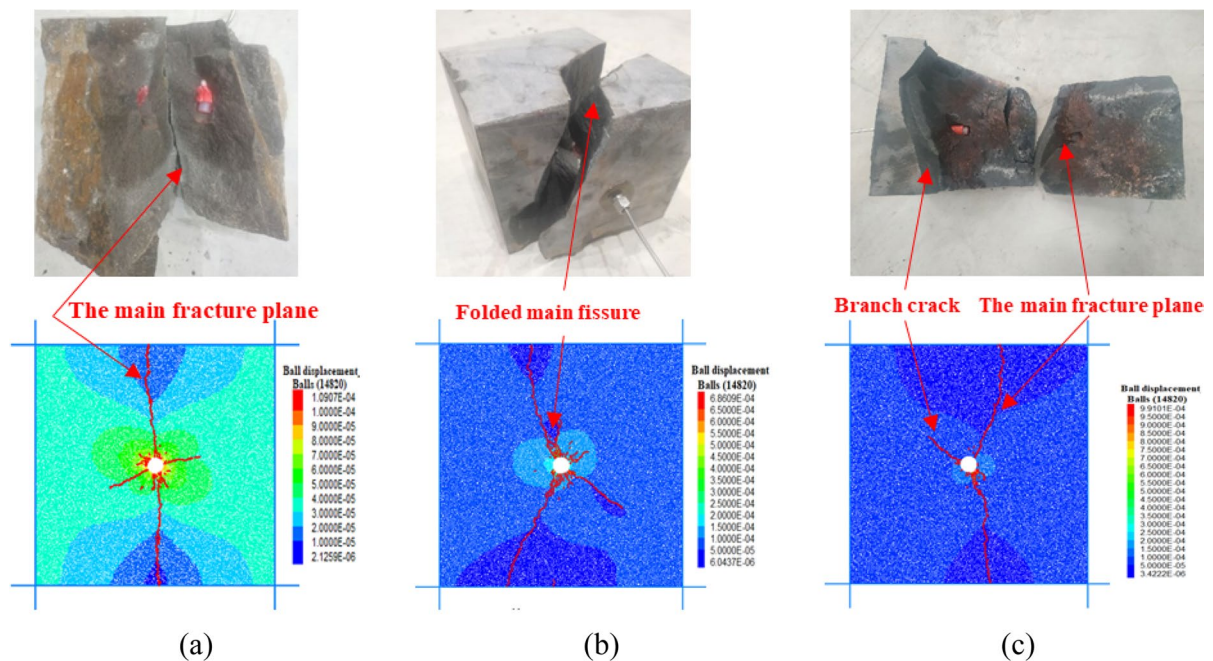

Fig. 12 Comparison between numerical calculation and laboratory test of rock fracture morphology: **a** $\sigma_H = \sigma_h = 5$MPa Unloading; **b** $\sigma_H = 5$MPa, $\sigma_h = 8$MPa No unloading; **c** $\sigma_H = 5$MPa, $\sigma_h = 8$MPa Unloading

Table 4 Micro parameters for fluid flow coupling model

Parameters	Values
Initial opening of pipeline a/mm	5×10^{-6}
When the aperture is reduced to half, Pressure F_0/Pa	5×10^{6}
Permeability coefficient k	1×10^{-14}
Opening reduction coefficient λ	0.2
Domain apparent volume V_d/mm^3	1
Fluid compression modulus K_f/Pa	3×10^{9}

Table 5 The conditions of hydraulic coupling simulation under the quasi-static unloading

Conditions	Initial stress/ MPa	The angle of water conducting crack θ/°
1–6	$\sigma_H = 5$, $\sigma_h = 2$	0, 15, 30, 45, 60, 90
7–12	$\sigma_H = \sigma_h = 5$	0, 15, 30, 45, 60, 90
13–18	$\sigma_H = 5$, $\sigma_h = 8$	0, 15, 30, 45, 60, 90
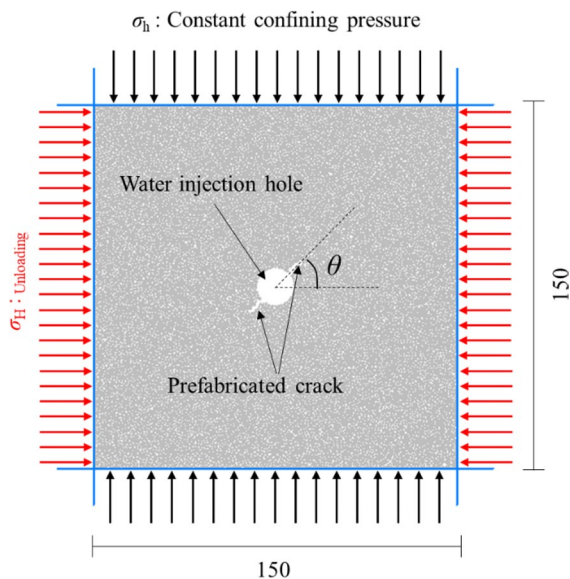
Fig. 13 Numerical simulation model of hydraulic coupling fracture of rock mass with prefabricated crack

water-conducting fracture. Still, it turns and extends along the horizontal direction (the direction of the maximum principal stress). Finally, a straight single tensile crack is formed. When $\theta = 45°$, affected by the singularity of water-conducting cracks tip, the hydraulic fracture is no longer a single through

fracture but branches in the expansion process and finally forms a "*Y*" type fracture morphology. The master fracture deflects to the horizontal direction under the induction of the maximum principal stress. However, the branch fracture is weakened by the induction of the maximum principal stress direction under the unloading condition and extends along the crack initiation direction to the model boundary. When $\theta = 60°$, the propagation direction of the main fracture is consistent with the angle of the water-conducting fracture, indicating that the induction effect of the principal stress at this angle can be neglected, and the angle of the water-conducting fracture plays a leading role. When $\theta = 90°$, the direction of the water-conducting fracture is perpendicular to the direction of the maximum principal stress. The main crack forms inclined cracks along the vertical direction, indicating that the induction of water-conducting cracks is greater than that of the principal stress difference. Therefore, when the angle φ between the water-conducting fracture and the direction of the maximum principal stress is less than 60°, the propagation direction of the hydraulic fracture is mainly controlled by the law of the maximum principal stress. When φ is greater than 60°, the propagation direction of the hydraulic fracture is controlled primarily by the angle of the water-conducting fracture.

In Fig. 14b, the initial principal stress σ_H is 5 MPa and σ_h is 5 MPa. When $0° \leq \theta \leq 30°$, the direction of the maximum principal stress gradually deviates from the direction of the water-conducting crack during the slow unloading process. However, the main fracture propagation direction is mainly along the horizontal direction (the direction of the water-conducting fracture). It indicates that the angle of the water-conducting crack more easily controls the hydraulic fracture propagation. When $\theta \geq 45°$, the principal stress difference is small at the initial stage of the main crack propagation, and the whole expands along the direction of water-conducting fracture. With the decrease of σ_H, the maximum principal stress direction is along the vertical direction. At this time, the hydraulic fracture is induced by the maximum principal stress and moves along the vertical direction, forming a concave crack. With the increase of θ, the radian of fracture decreases. When $\theta = 90°$, a single vertical fracture is formed under the joint control of the maximum principal stress and the water-conducting crack.

As shown in Fig. 14c, the principal stress difference increases gradually during unloading when the initial principal stress $\sigma_H = 5$ MPa and $\sigma_h = 8$ MPa. When $\theta < 30°$, the hydraulic fracture expands mainly along the horizontal direction, indicating that the water-conducting fracture's angle chiefly controls the main fracture propagation. In addition, a micro-fracture zone is formed above and below the water injection hole, affected primarily by the maximum principal stress. The water-conducting crack induces the formation of dominant expansion channels in the horizontal direction, so only some microfracture is formed in the vertical direction. When $\theta \geq 30°$, the hydraulic fracture propagation is mainly controlled by the direction of the maximum principal stress. An inclined single fracture is formed vertically, and the angle of the water-conducting crack has little effect on the propagation direction of the main crack.

For rock materials, the macroscopic strength and deformation characteristics during failure are closely related to the evolution of micro-structure. Therefore, the anisotropic evolution law of internal contact force after rock fracturing is further studied. The model is divided into an interval every $10°$ along the circumference of the hole, and the percentage of normal and tangential contact force in the average normal contact force in each interval is taken as the statistical object. This statistical data is used to draw a wind direction rose map, as shown by the solid blue line in Fig. 15. Rothenburg and Bathurst proposed that the Fourier function can be used to fit approximatively the evolving law of normal and tangential contact force between particles. The mathematical expressions are shown in Eqs. (1) and (2), and the curve obtained after fitting is shown the red line in Fig. 15.

$$f_n(\theta) = f_0 \left[1 + a_n \cos 2(\theta - \theta_n) \right] \tag{1}$$

$$f_t(\theta) = -f_0 a_t \sin 2(\theta - \theta_t) \tag{2}$$

In the above equations: f_0 is the average normal contact force relative to all contacts. θ_n and θ_t are the principal directions of normal and tangential contact force anisotropy, respectively. a_n and a_t are Fourier coefficients, and their values reflect the degree of anisotropy of the corresponding microfabric parameters.

As shown in Fig. 15a, when the initial principal stress $\sigma_H = 5$ MPa and $\sigma_h = 2$ MPa, the normal

contact force is distributed in a slender stick shape. When $\theta = 0°$, the degree of anisotropy is the highest, and the average normal contact force is the smallest. It indicates that the water pressure required for fracture is the smallest, the fracture surface is straight and smooth, and there are no other micro cracks. The tangential contact force is distributed in a centrosymmetric petal shape. The dominant direction of tangential contact force is close to that of normal contact force. When $\theta = 30°$, the average normal contact force is the largest, and the degree of anisotropy is the lowest. It indicates that rock fracturing is more difficult at this angle, the degree of internal damage is higher, and the degree of force balance between particles is lower.

As shown in Fig. 15b, when the initial principal stress $\sigma_H = \sigma_h = 5$ MPa, the principal stress difference gradually increases under the unloading action. However, at the initial stage of crack propagation, the induction effect in the direction of the maximum principal stress is much less than that of the water-conducting crack. The hydraulic fracture expands along the direction of the water-conducting crack. Therefore, the normal and tangential contact force also has obvious directionality, and the dominant principal direction of the contact force is approximately perpendicular to the angle of the water-conducting fracture. The average normal contact force increases gradually with the increase of water-conducting fracture angle θ. This is mainly due to the gradual convergence between the water conduction fracture angle and the direction of the maximum principal stress, and the normal contact force increases under the combined action of the two. The anisotropy coefficient of rock mass at $0° \leq \theta \leq 30°$ is about twice that at $\theta \geq 60°$. It shows that when the angle of the water-conducting crack deviates from the direction of the maximum principal stress, the degree of anisotropy after fracturing is higher, and the internal stress changes more violently.

It can be seen from Fig. 15c that when the initial principal stress $\sigma_H = 5$ MPa and $\sigma_h = 8$ MPa, under the high principal stress difference, the dominant direction of normal and tangential contact force is roughly along the vertical direction. When $\theta \geq 30°$, the dominant direction deviates slightly, and the normal contact force changes little under the different angles of the water-conducting crack, indicating that the water-conducting crack had little effect on the contact force. When $\theta \geq 60°$, the normal and tangential anisotropy
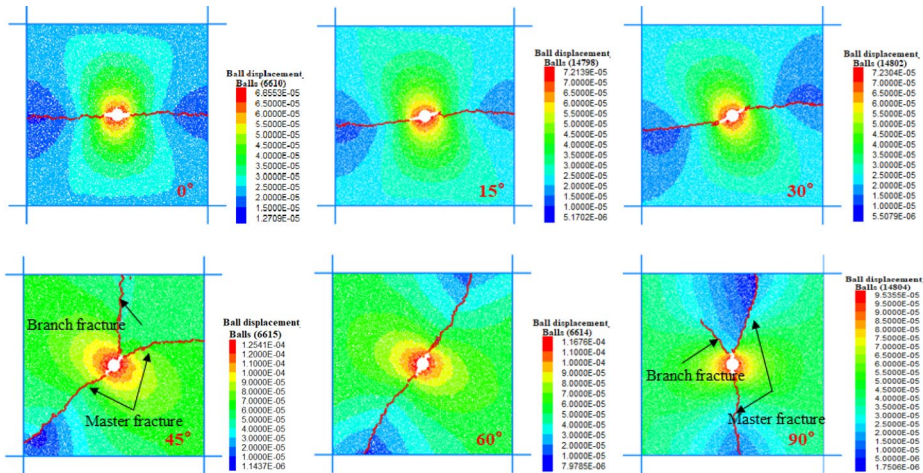
(a)
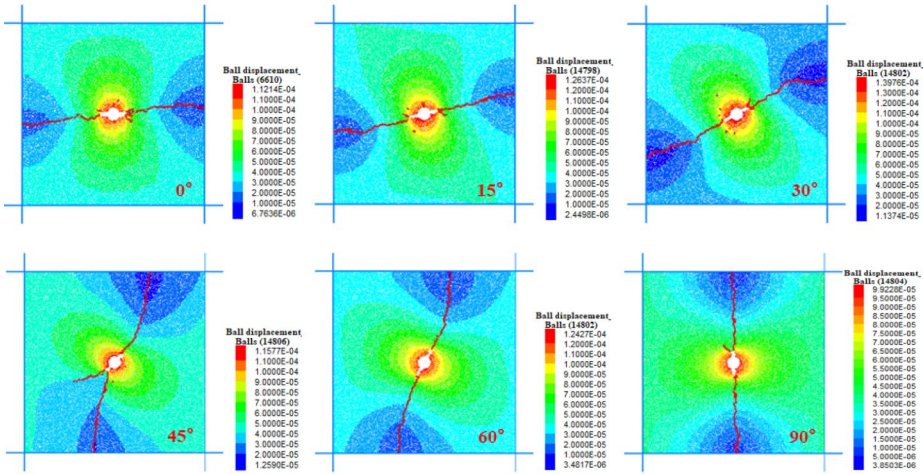
(b)
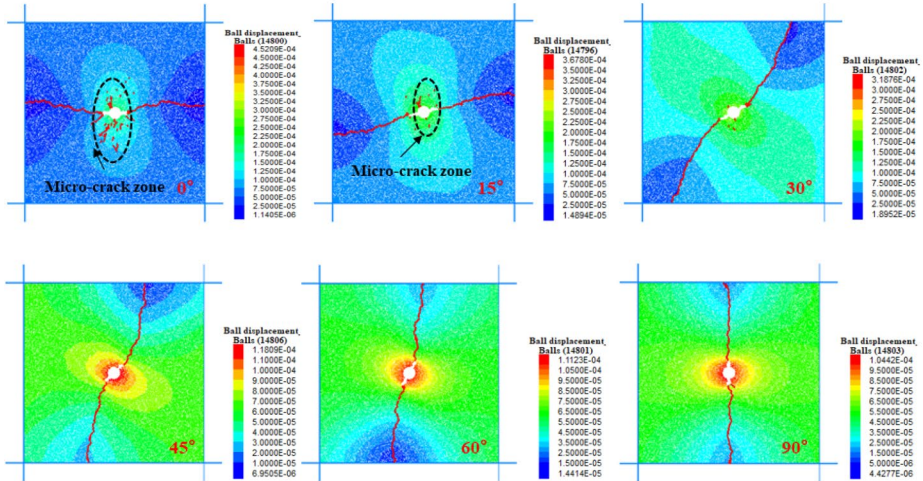
(c)

◄**Fig. 14** Fracture propagation morphology under different water-conducting fracture angles: **a** Initial principal stress $\sigma_H = 5MPa$, $\sigma_h = 2MPa$; **b** Initial principal stress $\sigma_H = 5MPa$, $\sigma_h = 5MPa$; **c** Initial principal stress $\sigma_H = 5MPa$, $\sigma_h = 8MPa$

coefficients are small, which is about half of that when $\theta \leq 30°$. It shows that the degree of anisotropy is greatly affected by the angle of the water-conducting crack. When θ is consistent with the maximum principal stress direction, the degree of anisotropy is lower.

5.2 Influence of Water-Conducting Cracks' Angle on the Internal Stress

By setting several measuring circles of the same size in the model to monitor the internal stress changes of rock mass fracture under different θ, it can be used to reveal the stress field evolution law of rock mass fracture under the influence of θ.

It can be seen from Fig. 16 that the horizontal and vertical stresses inside the model exhibit a significant single peak distribution after rock mass fracture, and the stress around the hole is the largest. As the distance from the water injection hole increases, the internal stress of the model decreases rapidly and finally tends to be stable. When the initial principal stress $\sigma_H = 5$ MPa and $\sigma_h = 2$ MPa, the variation pattern of horizontal and vertical stress in the model under different θ is shown in Fig. 16a. When $\theta < 45°$, the horizontal stress increases gradually with the increase of θ. It shows that with the increase of the deviation between the angle of the water-conducting fracture and the direction of the maximum principal stress, the water pressure required for the fracture of the model is greater. The vertical stress changes little because the hydraulic fracture mainly spreads along the horizontal direction. When $\theta > 45°$, the angle of the water-conducting crack deviates more from the direction of the maximum principal stress, showing that the water pressure required by the model fracturing is higher. But with the increase of θ in this interval, the horizontal stress changed little. In contrast, the vertical stress shows a noticeable gradient change, mainly because the hydraulic fracture spread along the vertical direction. When $\theta = 45°$, the horizontal and vertical stresses of the model are at the maximum. Therefore, when $\theta = 45°$, the water pressure

required for rock fracture is greater, making it more difficult to achieve fracturing.

When the initial principal stress $\sigma_H = \sigma_h = 5$ MPa, the variation pattern of horizontal and vertical stress in the model under different θ is shown in Fig. 16b. The following results can be obtained with the hydraulic fracture propagation pattern in Fig. 14b. When $0° \leq \theta \leq 30°$, the hydraulic fracture spread along the horizontal direction, and the horizontal stress increased gradually with the increase of θ. When $\theta = 30°$, the stress is the largest, controlled by the angle of the water-conducting fracture and the principal stress. The direction of the maximum principal stress deviates from the angle of the water-conducting fracture, which has a certain inhibitory effect on crack propagation. When $45° \leq \theta \leq 90°$, the hydraulic fracture spreads along the vertical direction. With the increase of θ, the vertical stress decreased gradually. In this case, the direction of the maximum principal stress is consistent with the angle of the water-conducting crack. Under the joint induction of both, the water pressure required for the hydraulic fracture expansion was smaller, and the fracture was more likely to occur.
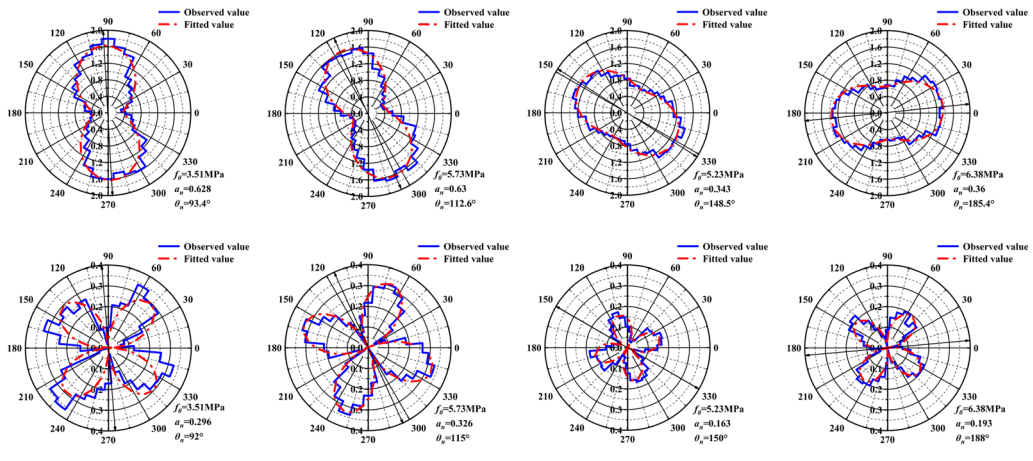
When the initial principal stress $\sigma_H = 5$ MPa and $\sigma_h = 8$ MPa, the variation pattern of horizontal and vertical stress in the model under different θ is shown in Fig. 16c. The analysis results are as follows by combining Fig. 16c, 14c. When $0° \leq \theta \leq 15°$, the hydraulic fracture spreads along the horizontal direction. As θ increases, the horizontal stress increases slightly without significant overall disparity. When $30° \leq \theta \leq 90°$, the hydraulic fracture spreads in the vertical direction. The law of vertical stress is similar to Fig. 16b. With the increase of θ, the vertical stress of the model decreases gradually. But in Fig. 16b, the maximum stress occurs when $\theta = 30°$, and the hydraulic fracture migrates vertically during propagation. It shows that under a high principal stress difference, the induction effect of the maximum principal stress on hydraulic fracture is much more significant than that of the water-conducting crack.

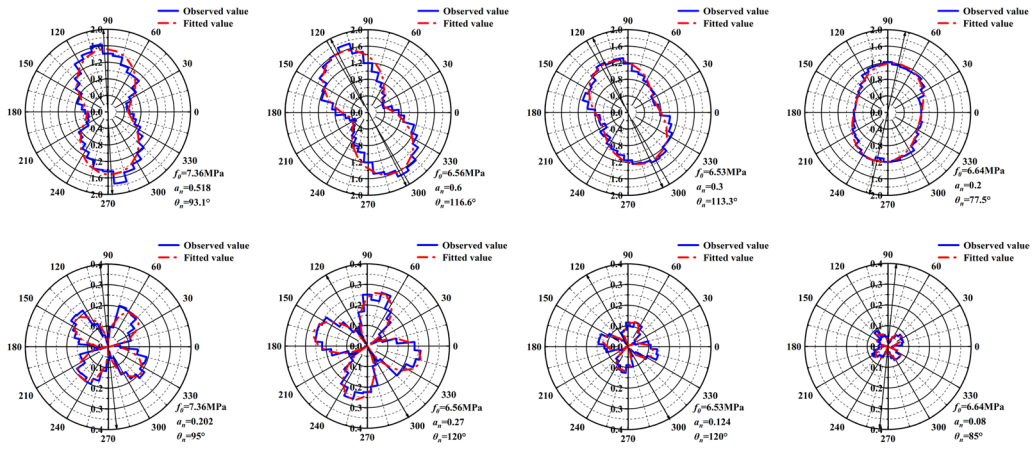## 5.3 Influence of Water-Conducting Cracks' Angle on the Fracture Pressure

The rock mass is unloaded at different initial principal stresses until it breaks at constant water pressure, at which point the water pressure is the fracture pressure
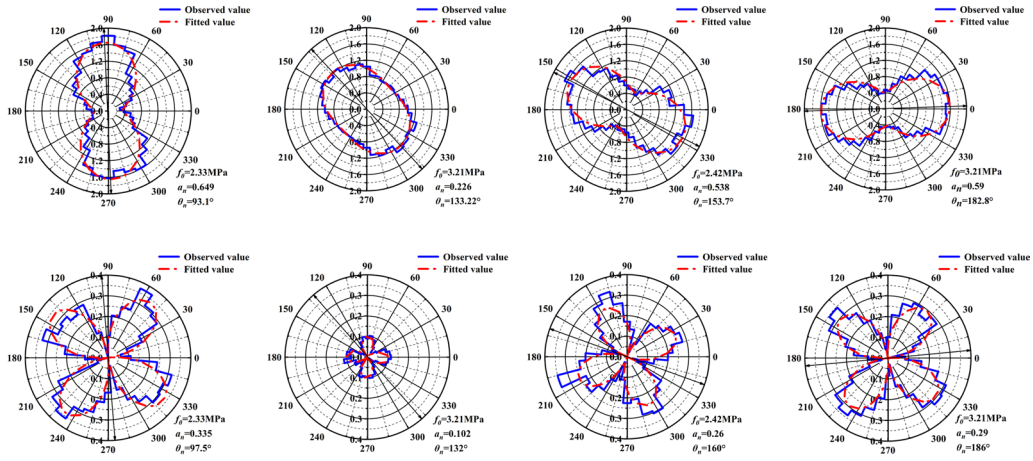
(a)

(b)

(c)

◄**Fig. 15** Normal and tangential contact force rose diagram of model at 0°、30°、60°、90° water conduction fracture Angle: **a** Initial principal stress $\sigma_H = 5$MPa, $\sigma_h = 2$MPa; **b** Initial principal stress $\sigma_H = 5$MPa, $\sigma_h = 5$MPa; **c** Initial principal stress $\sigma_H = 5$MPa, $\sigma_h = 8$MPa

of the rock mass during the unloading. Therefore, it is significant to study the variation law of fracture pressure of rock mass under different angles of water-flowing fracture(θ) to reveal the bearing characteristics of water-resisting rock mass under unloading.

The curves in Fig. 17 are the fracture pressure of rock mass under different angles of θ, obtained by unloading step by step under three different initial principal stresses. By analyzing the curve in Fig. 17, the following rules are obtained. When the initial principal stress $\sigma_H = 5$ MPa and $\sigma_h = 2$ MPa, with the increase of θ, the fracture pressure of rock mass increases as a whole. The fracture pressure is the highest when $\theta = 45°$, which is consistent with the previous conclusion. When $\theta < 45°$, it is controlled by the maximum principal stress, the angle of the water-conducting crack is consistent with the direction of the maximum principal stress, and the fracture pressure is slight. When $\theta > 45°$, the angle of the water-conducting crack mainly controls the direction of fracture propagation. However, the direction of maximum principal stress restrains it, and the fracture pressure is higher.

When the initial principal stress $\sigma_H = \sigma_h = 5$ MPa, there is little difference in rock mass fracture pressure under different θ. When $0° \leq \theta \leq 30°$, the rock mass fracture pressure first decreases and then increases. When $30° \leq \theta \leq 90°$, with the increase of θ, the rock fracture pressure decreases gradually. The fracture pressure is the highest when $\theta = 30°$, consistent with the conclusion obtained in Sect. 5.2, indicating that the maximum principal stress substantially inhibits hydraulic fracture propagation at this angle.
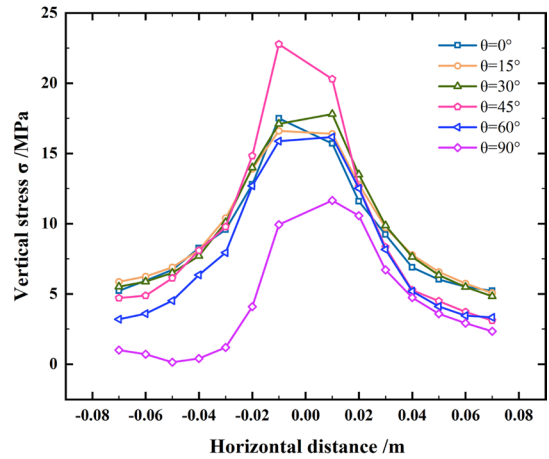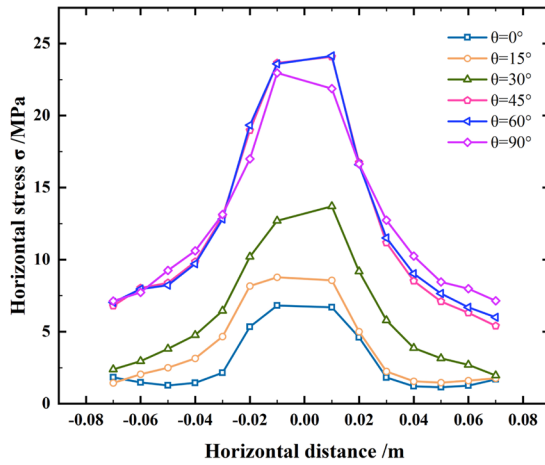
When the initial principal stress $\sigma_H = 5$ MPa and $\sigma_h = 8$ MPa, with $\theta = 30°$ and $\theta = 60°$ as the demarcation point, the variation of fracture pressure with θ is roughly divided into three intervals. The fracture pressure changes little when $0° \leq \theta \leq 30°$ and $60° \leq \theta \leq 90°$, but the fracture pressure of θ ranging from 0° to 30° is about twice that of θ ranging from 60° to 90°. It indicates that rock mass fracture is more difficult under low water-conducting cracks' angles, mainly due to the deviation between the angle of the

water-conducting crack and the direction of the maximum principal stress. However, when $30° \leq \theta \leq 60°$, with the angle of hydraulic fracture gradually moving towards the maximum principal stress, the effect of maximum principal stress on rock mass fracture becomes more pronounced. When $\theta \geq 60°$, the maximum principal stress has the greatest inducing effect on the propagation of hydraulic fracture and is no longer affected by the angle of the water-conducting crack.

6 Conclusions

Based on laboratory tests and discrete element numerical simulation methods, this paper studies the hydraulic fracture characteristics of rock mass under unloading conditions. It analyzes the expansion mechanism and failure mode of hydraulic fracture of rock mass under different working conditions. The following conclusions are drawn:

1. When the initial principal stress is 0, the failure mode of rock mass under slow unloading is a multi-crack cutting failure, and the hydraulic fracture deflects in the expansion process with the slow increase of principal stress difference. The failure mode of rock mass under rapid unloading is a tension-shear failure, and the failure mode is greatly affected by the principal stress difference. From the point of view of fracture pressure, slow unloading requires higher water pressure. But the fracture time is shorter, and the energy release rate is greater at the moment of failure.
2. When the initial principal stress $\sigma_H < \sigma_h$, the failure mode of rock mass is single crack splitting failure under slow unloading, while under rapid unloading, the failure mode of rock mass is a multi-crack cutting failure, and the fracture surface is tortuous and complex. From the point of view of fracture pressure, with the increase of unloading rate, the fracture pressure of rock mass gradually decreases.
3. The influence of water-conducting fractures on the crack propagation of rock mass is as follows. When the principal stress difference is low and the unloading rate is low, the propagation direction of the hydraulic crack is mainly controlled by the direction of maximum principal stress

(a)
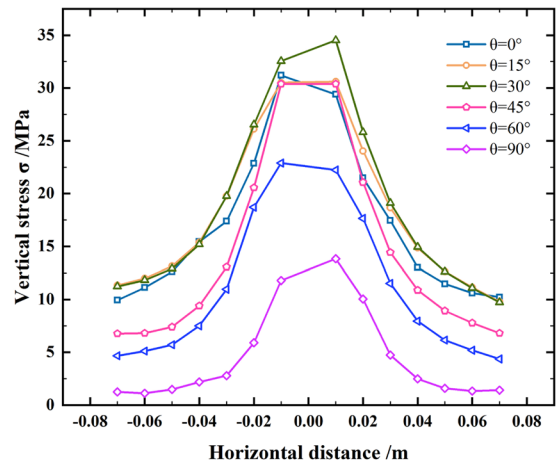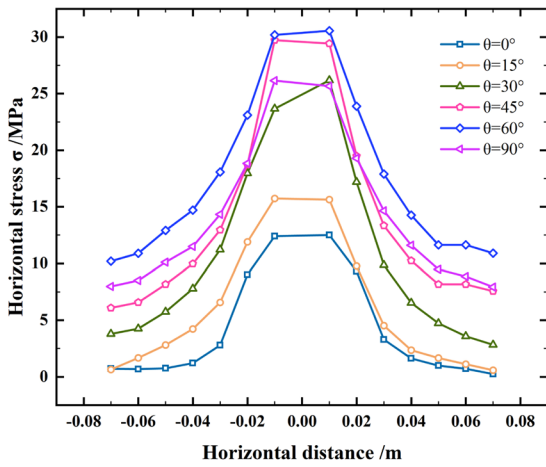
(b)
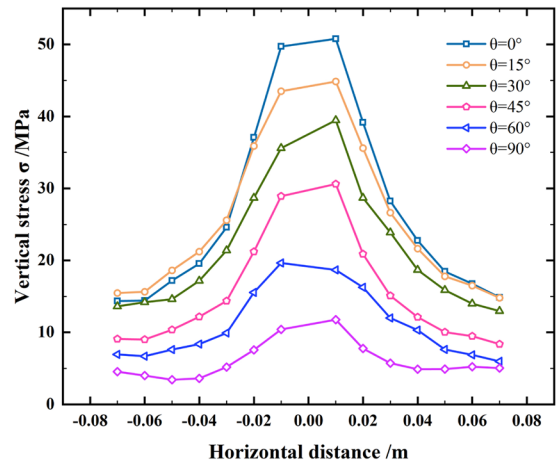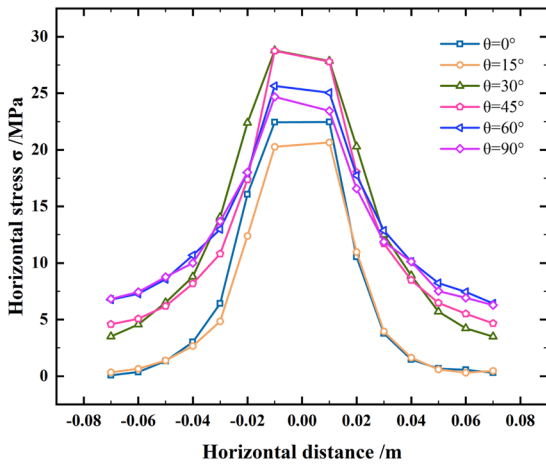
(c)

◄**Fig. 16** The variation of horizontal and vertical stress in the model under different water-conducting fracture angles: **a** Initial principal stress $\sigma_H = 5$MPa, $\sigma_h = 2$MPa; **b** Initial principal stress $\sigma_H = 5$MPa, $\sigma_h = 5$MPa; **c** Initial principal stress $\sigma_H = 5$MPa, $\sigma_h = 8$MPa

at $\theta < 45°$; it is controlled by the angle of water diversion fissure at $\theta > 45°$. When the principal stress difference is high and the unloading rate is low, the propagation of hydraulic fracture is mainly controlled by the direction of maximum principal stress at $\theta \geq 30°$, and the angle of water-conducting fracture has little effect on the propagation direction of the main fracture.

4. Based on the wind direction rose map of contact force and the stress change of the model, the induction mechanism of the maximum principal stress and the water-conducting fracture angle is clarified. Under the condition of low principal stress difference, when the angle of water-conducting fracture deviates from the direction of maximum principal stress, the anisotropy of the model after fracturing is higher. Under a high principal stress difference, the dominant direction of contact force is mainly controlled by the maximum principal stress direction. The angle of the water-conducting fissure can shift slightly in the dominant direction. The angle of the water-conducting fracture greatly affects the degree of anisotropy.
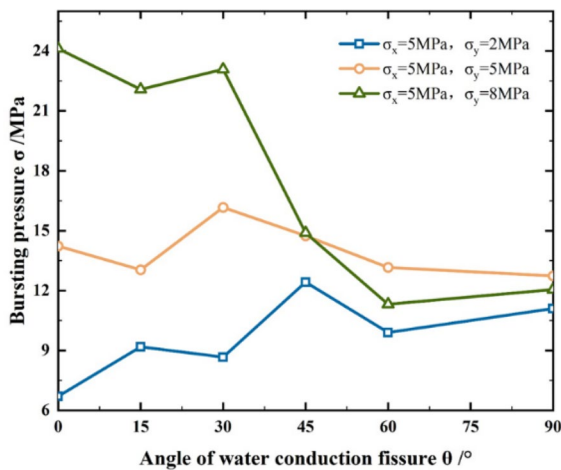

Fig. 17 The fracture pressure under different θ

Author Contributions All authors contributed to the study conception and design; JY: Investigation, Validation, Formal analysis, Methodology, Writing-original draft; MW: Methodology, Data curation, Visualization, Investigation, Project administration; ZZ: Conceptualization, Funding acquisition, Data curation, Visualization; WY: Visualization, Investigation, Supervision, Funding acquisition; SB: Validation, Formal analysis, Conceptualization; DZ: Writing-review & editing, Visualization, Formal analysis; GY: Data Curation; PJ: Supervision, Resources, Software; XJ: Supervision, Software; PL: Resources.

Code Availability All code generated or used during the study are proprietary or confidential in nature and may only be provided with restrictions.

Declarations

Conflict of interest The authors declare that they have no known competing financial interests or personal relationships that could have appeared to influence the work reported in this paper.

References

Abdollahi S, Madadi M, Ostad-Ali-Askari K (2021) Monitoring and investigating dust phenomenon on using remote sensing science, geographical information system and statistical methods. Appl Water Sci 11:111

Cao J, Shi ST (2023) Evolution Law of Mining-induced Fractures in Shallow Buried Close Coal Seams Mining. Geotech Geol Eng 2023:1–12

Cordero J, Sanchez CM, Quevedo R (2020) Impacts of natural fractures on hydraulic fracturing treatment in all asymptotic propagation regimes. Comput Method Appl M 371:113296

Duan HQ, Xiong S, Yu WB (2023) Numerical simulation study on mechanical and acoustic emission characteristics of coal–rock combined body subjected to cyclic disturbing loading. Geotech Geol Eng 41:783–802

Evbuomwan PO, Yu DM (2011) Theoretical and practical risk assessment method in tunneling. Adv Mater Res 255–260:3953–3957

Fan HY, Li LP, Zong PJ, Liu HL, Yang LJ, Wang J, Yan P, Sun SQ (2023) Advanced stability analysis method for the tunnel face in jointed rock mass based on DFN-DEM. Undergr Space 13:136–149

Gao CL, Li SC, Wang J, Li LP, Lin P (2018) The risk assessment of tunnels based on grey correlation and entropy weight method. Geotech Geol Eng 36:1621–1631

Huang X, Liu QS, Liu KD, Kang YS, Liu XWi, (2015) Laboratory study of deformation and failure of soft rock for deep ground tunneling with TBM. Chin J Rock Mech Eng 34(1):76

Jiang Q, Zhang MZ, Yan F, Su GH, Feng XT, Xu DP, Feng GL (2020) Effect of initial minimum principal stress and unloading rate on the spalling and rockburst of marble: a true triaxial experiment investigation. B Eng Geol Environ 80(2):1617–1634

Li JL, Wang LH, Wang XX, Wang RH, Cheng Z, Li D (2010) Research on unloading nonlinear mechanical characteristics of jointed rock masses. J Rock Mech Geotech 2(4):357–364

Li LP, Hu J, Li SC, Qin CS, Liu HL, Chen DY, Wang J (2021a) Development of a novel triaxial rock testing method based on biaxial test apparatus and its application. Rock Mech Rock Eng 54:1597–1607

Li SC, Liu C, Zhou ZQ, Li LP, Shi SS, Yuan YC (2021b) Multi-sources information fusion analysis of water inrush disaster in tunnels based on improved theory of evidence. Tunn Undergr Sp Tech 113:103948

Liang DX, Jiang ZQ, Zhu SY, Sun Q, Qian ZW (2016) Experimental research on water inrush in tunnel construction. Nat Hazards 81(1):467–480

Liu ZY, Wang SJ, Zhao HY, Li W, Li W, Geng YD, Tao S, Zhang GQ, Chen M (2017) Effect of random natural fractures on hydraulic fracture propagation geometry in fractured carbonate rocks. Rock Mech Rock Eng 51(3):1–21

Liu SL, Zhu QZ, Shao JF (2020) Deformation and mechanical properties of rock: effect of hydromechanical coupling under unloading conditions. B Eng Geol Environ 79(10):5517–5534

Ma G, Zhang F, Liu X, Feng D, Zhang PW (2016) Experimental study of impact of crustal stress on fracture pressure and hydraulic fracture. Rock Soil Mech S2:7

Ren QS, Jiang YD, Wang PP, Wu GJ, Nima ND (2021) Experimental and Numerical Simulation Study of Hydraulic Fracture Propagation during Coalbed Methane Development. Geofluids 3632997:1–12

Sivakumar G, Maji VB (2023) Study on crack growth behaviour in rocks having pre-existing narrow flaws under biaxial compression. Geotech Geol Eng 41:153–188

Talebmorad H, Ostad-Ali-Askari K (2022) Hydro geo-sphere integrated hydrologic model in modeling of wide basins. Sust Wat Resour Man 8:118

Wang S, Li LP, Cheng S, Hu HJ, Zhang MG, Wen T (2020) Risk assessment of water inrush in tunnels based on attribute interval recognition theory. J Cent South Univ 27(2):517–530

Yang WM, Geng Y, Zhou ZQ, Li LC, Ding RS, Wu ZH, Zhai MY (2020) True triaxial hydraulic fracturing test and numerical simulation of limestone. J Cent South Univ 27(10):3025–3039

Yin GZ, Ma B, Liu C, Li MH, Lu J, Yin SY (2019) Effect of loading and unloading rates on mechanical properties and energy characteristics of sandstone under true triaxial stress. J China Coal Soc 44(2):454–462

Zhang JW, Song ZX, Wang SY (2021) Experimental investigation on permeability and energy evolution characteristics of deep sandstone along a three-stage loading path. B Eng Geol Environ 80(2):1571–1584

Zhang DJ, Wang JD, Guo S, Cao JL (2022) Research on the underground water inrush mechanism based on the influence of fault. Geotech Geol Eng 40:3531–3550

Zhao NY, Jiang HF (2021) Mathematical methods to unloading creep constitutive model of rock mass under high stress and hydraulic pressure. Alex Eng J 60(1):25–38

Zhao GB, Guo WB, Kong LY, Zhao Y, Shi QW (2022) Couple effect of joint pore pressure and joint orientations on rock strength based on numerical modeling. Geotech Geol Eng 40:5397–5409

Zhou ZL, Zhao JP, Tan ZS, Zhou XP (2021) Mechanical responses in the construction process of super-large cross-section tunnel: a case study of Gongbei tunnel. Tunn Undergr Sp Tech 115(4):104044

Zhu JQ (2020) Li TZ (2020) Catastrophe theory-based risk evaluation model for water and mud inrush and its application in karst tunnels. J Cent South Univ 27(5):1587–1598

Zou YS, Ma XF, Zhang SC, Zhou T, Li H (2016) Numerical investigation into the influence of bedding plane on hydraulic fracture network propagation in shale formations. Rock Mech Rock Eng 49(9):3597–3614